Model of remote-sensing reflectance including bidirectional effects for case 1 and case 2 waters

Young-Je Park and Kevin Ruddick

A remote-sensing reflectance model based on a lookup table is proposed for use in analyzing satellite ocean color data in both case 1 and case 2 waters. The model coefficients are tabulated for grid values of three angles—solar zenith, sensor zenith, and relative azimuth—to take account of directional variation. This model also requires, as input, a phase function parameter defined by the contribution of suspended particles to the backscattering coefficient. The model is generated from radiative transfer simulations for a wide range of inherent optical properties that cover both case 1 and 2 waters. The model uncertainty that is due to phase function variability is significantly reduced from that in conventional models. Bidirectional variation of reflectance is described and explained for a variety of cases. The effects of wind speed and cloud cover on bidirectional variation are also considered, including those for the fully overcast case in which angular variation can still be considerable (~10%). The implications for seaborne validation of satellite-derived water-leaving reflectance are discussed.

OCIS codes: 010.4450, 280.0280, 290.1350, 010.7340.

1. Introduction

In this study we describe a model of remote-sensing reflectance as a function of inherent optical properties and of Sun–sensor viewing geometry that is valid for both case 1 and case 2 waters, thus extending the works of Morel and Gentili[1] and Morel *et al.*[2]

Models that express water reflectance as a function of the absorption coefficient (a) and the backscattering coefficient (b_b) are used for analysis and processing of ocean color data.[3–6] The two most widely used expressions of the subsurface remote-sensing reflectance, r_{rs}, defined by the ratio of upwelling radiance $[L_u(0^-)]$ to downwelling irradiance $[E_d(0^-)]$ just below the sea surface, are[4,7]

$$r_{rs} = l_1 \frac{b_b}{a + b_b} + l_2 \left(\frac{b_b}{a + b_b} \right)^2 \tag{1}$$

$$r_{rs} = \frac{f}{Q} \frac{b_b}{a} = \frac{f'}{Q} \frac{b_b}{a + b_b}, \tag{2}$$

where $(l_1, l_2) = (0.0949, 0.0794)$ and the value of f/Q depends on the viewing geometry, with an average of 0.0922 for remote-sensing cases. These model equations are based on radiative transfer simulations with various water optical properties and solar zenith angles, though they are designed primarily for low reflectances ($b_b \ll a$). Lee *et al.*[8] have noted that the difference between the two models becomes significant for high reflectance.

In most remote-sensing applications, the angular dependence of the remote-sensing reflectance is ignored. Constant values have been employed for coefficients l_1 and l_2 in Eq. (1) or f/Q in Eq. (2) regardless of the positions of Sun and sensor. However, it has been shown that the f/Q factor varies with Sun and sensor angles (the solar zenith angle, the satellite zenith angle, and the relative azimuth angle), indicating that water's reflectance is bidirectional.[1,7] This bidirectional property needs to be accounted for if highly accurate water reflectance data are required, for example in the vicarious calibration or sea-level validation of satellite sensors. Morel and Gentili[7] have shown that the bidirectional property depends on the inherent optical properties (IOPs) of the water body as well as on the angles of Sun and sensor. For remote-sensing applications they parameterized the f/Q factor as a function of chlorophyll concentration (Chl) in case 1 waters.[1,2] However, in case 2 waters, by definition the IOPs are not determined by Chl alone because of the presence of other suspended particles that do not covary with Chl, and a case 1 water

The authors are with the Management Unit of the North Sea Mathematical Models, Royal Belgian Institute of Natural Sciences, Gulledelle 100, Brussels 1200, Belgium. Y.-J. Park's e-mail address is y.park@mumm.ac.be.

Received 17 March 2004; revised manuscript received 4 October 2004; accepted 29 October 2004.

0003-6935/05/071236-14$15.00/0

model for bidirectional effects is clearly not applicable. Even in case 1 waters, it has been reported that the scattering coefficient may not be well correlated with *Chl*.[9] Loisel and Morel[10] studied the bidirectional upward radiance field for two contrasting case 2 waters: sediment-dominated and yellow-substance-dominated waters. A practical approach to describing the bidirectional water reflectance was proposed that used an *a priori* classification of a region as either turbid water or yellow-substance-dominated water, though no solution was offered for water with an intermediate mixture of sediments and dissolved colored material. Recently Albert and Mobley[11] proposed an analytical model for the subsurface remote-sensing reflectance, which accounts for the directional variation. Their study is based on radiative transfer simulations that used optical properties typical of Lake Constance (case 2 waters), including a Petzold-type phase function. Improved model accuracy was shown by inclusion of Sun zenith, sensor zenith, and wind speed as input parameters. However, this model does not include the relative azimuth angle dependence, which is important for describing the bidirectional variation as shown by Morel and his collaborators,[1,2,7] nor is there a possibility for variable phase function as may be needed to describe accurately the bidirectional water reflectance for various mixtures of *Chl*, nonalgae particles, and yellow substance. Therefore it is necessary to extend the existing theory for bidirectional reflectance to a general water body and thus to applications in coastal case 2 waters as well as case 1 waters.

In this study we aim to present a model of the remote-sensing reflectance (R_{rs}) that accounts for the bidirectional variation of diverse water types including turbid and absorbing waters. The model coefficients are tabulated for grid values of the Sun and sensor angles to incorporate the directional variation. Furthermore, a parameter γ_b, defined as the particle fraction of total backscattering, is introduced as an input parameter of the model. This parameter is an indicator of the shape of the scattering phase function (SPF) and is important in shaping the directional distribution of the water-leaving radiance. The model coefficients are obtained with simulated R_{rs} data. Radiative transfer computations are carried out for a wide range of IOPs, a and b_b, and for realistic conditions of the solar zenith angle in addition to the overcast case, which is included for airborne and seaborne remote sensing. Wavelength ranges from visible to near infrared (412 to 780 nm) are simulated. In turbid waters, the red and near-infrared reflectances are useful for retrieval of chlorophyll[6] and suspended particulate matter[12,13] and for atmospheric correction.[12,14]

In this model, transspectral effects such as Raman scattering, and colored dissolved organic matter–chlorophyll fluorescence are not considered.

In Section 2 the equation for the R_{rs} model is formulated, starting with the quasi-single-scattering approximation and then generalizing to include multiple-scattering effects. This model is written in a form suitable for inversion, i.e., retrieval of IOPs from measured reflectance. In Section 3 the simulation conditions—the IOPs (absorption, scattering, and scattering phase function), the Sun and sensor angles, and the wind speed—are described. In Section 4 the model error is given and is analyzed in terms of variability of the phase function. Examples of the bidirectional distribution of R_{rs} are also presented, including the effects of wind speed and cloud coverage. In Section 5 a comparison with conventional models is discussed, and the accuracy of the b_b estimation required for exploiting the proposed model is assessed.

2. Model Formula (from the Quasi-Single-Scattering Approximation)

The quasi-single-scattering approximation[15] (QSSA) is valid when single-scattering events are dominant and scattering occurs strongly in the forward direction. The QSSA assumes that the forward-scattered photons are not removed from the incident beam. Its analytical expression gives important insight for modeling the remote-sensing reflectance. For homogeneous and deep waters without an intervening atmosphere, the subsurface remote-sensing reflectance according to the QSSA will be

$$r_{rs}(\theta_o', \ \theta', \ \Delta\phi) = \frac{1}{\cos\theta_o' + \cos\theta'} \frac{b}{b_b} P(\Theta) \frac{b_b}{a + b_b}, \tag{3}$$

where θ_o', θ', and $\Delta\phi'$ are the solar and sensor zenith and relative azimuth angles in the water, respectively, and $P(\Theta)$ is the SPF at scattering angle Θ, which is related to Sun and sensor angles by $\cos\Theta = \sin\theta_o' \sin\theta' \cos\Delta\phi' + \cos\theta_o' \cos\theta'$. The factor $bP(\Theta)/b_b$ is the SPF normalized to a backscattering ratio (NSPF), and its integration over the backscattering hemisphere gives 1. This NSPF represents the phase function contribution to the bidirectional variation of r_{rs} in the limit of single scattering. The factor $b_b/(a + b_b)$ is an angle-independent factor that determines the water reflectance, which represents the probability of backscattering per extinction event when the QSSA is valid, i.e., when the forward-scattered photons are considered not to be removed from the incident beam. In this paper it is called backscattering albedo and is denoted ω_b hereafter.

The expression for the remote-sensing reflectance above the surface, R_{rs}, can be obtained by addition of the sea-surface interface term[4] to Eq. (3):

$$R_{rs} = \frac{(1 - \rho)(1 - \bar{\rho})}{n_w^2(1 - \bar{r}R)} r_{rs}, \tag{4}$$

where ρ is the surface reflectance for upward radiance, $\bar{\rho}$ is the surface reflectance for downward irradiance; n_w is the refractive index of seawater, $\bar{r}$ is the surface reflectance for diffused upward irradiance, and R is the irradiance reflectance just below the

surface. In this form the sea-surface term depends on the IOP through R and $\bar{r}$, a factor that cannot be neglected for turbid waters if high accuracy is required. Modeling of R_{rs} is more useful than modeling of r_{rs} because the latter would require an additional model of air–sea interface effects for application to remote-sensing data. Modeling of R_{rs} rather than r_{rs} is therefore preferred in this study.

Remote-sensing reflectance was defined theoretically as the ratio of the normalized water-leaving radiance and extraterrestrial solar irradiance. This definition yields a quasi-inherent optical property corrected for the effect of atmosphere and the viewing geometry.[16] However, in practice, this term is computed by division of the water-leaving radiance (after removal of air–water interface reflection) by the downwelling irradiance at just above the surface and varies bidirectionally. In this study the latter definition of remote-sensing reflectance, not corrected for the bidirectional effects, is used. Assuming that $\bar{r}R \ll 1$, Eq. (4) can be factored as follows:

$$R_{rs} = (\text{surface and angular factor}) \times (\text{phase function factor})\omega_b. \quad (5)$$

The surface and angular factor depends primarily on the Sun and sensor angles and, to a lesser extent, on wind speed and the illuminating radiance distribution. The phase function factor is determined by contributions from pure water and suspended particles. Whereas the pure-water contribution is constant at a given wavelength, the particle contribution is approximately proportional to particle concentration and varies with the optical properties of particles, such as refractive index and particle size distribution. In principle, the particle contribution could be modeled if the relative concentration of component particles such as phytoplankton, detritus, and terrigenous particles were known. However, it is not feasible to quantify the contribution of each scatterer type from remote-sensing data.

As far as remote sensing (thus backward scattering) is concerned, the phytoplankton contribution to the particle SPF is relatively small compared to the contribution of the smaller nonalgae particles for most realistic cases because of the small backscatter efficiency.[17,18] Assuming that the detritus NSPF is approximately the same as that of other terrigenous particles, a single particle NSPF can be used for all suspended particles (although in the present study this NSPF is allowed to vary as function of ω_b, as will be seen later). With this assumption of a single particle NSPF, the total NSPF can be specified by means of the relative strength of particle and pure-water scattering. Because the backward scattering can be retrieved more easily from the remote-sensing data than can total scattering, the phase function indicator in the present model is expressed in terms of backscatter quantities. So the phase function parameter, γ_b, is defined as the particle fraction of backscatter ($\gamma_b \equiv b_{bp}/b_b$, where b_{bp} is the backscatter coefficient for all particles) and is used to determine the SPF in this model. This γ_b parameter varies over a wide range from 0.2 to 1 because the particle contribution to backscatter is highly variable.[19] In Section 3 it is shown that the particle NSPFs differ by as much as a few percent for backscatter directions. This variation of the particle NSPF for given ω_b and γ_b parameters is a source of uncertainty of the model prediction, as we discuss below.

To incorporate multiple-scattering effects as well as the variation of particle NSPF with ω_b, we added higher-order terms to Eq. (5). As the fitting equation for the simulated R_{rs} as function of ω_b a polynomial was considered:

$$R_{rs}(\theta_o, \theta, \Delta\phi) = \sum_{i=1}^{4} g_i(\theta_o, \theta, \Delta\phi, \gamma_b)\omega_b^{\,i}, \quad (6)$$

where g_i are coefficients that are computed for solar zenith angle θ_o, sensor zenith angle θ, and relative azimuth angle $\Delta\phi$. A fourth-order polynomial was chosen such that the numerical fitting error can be much smaller than a typical directional variation of R_{rs} of 10%. This polynomial gave a fitting error smaller than 1–2%. However, such a high-order polynomial does not behave smoothly outside the range of ω_b used for fitting and may cause unwanted error if it is used for a range of ω_b that is not covered by simulation. To prevent this error from occurring, some unrealistic cases with small water absorption were added to extend the range of ω_b to 0.5.

Wavelength is not an explicit variable of this model, and the model is thus generic in this respect, although wavelength is required for computing absorption coefficient a, backscatter coefficient b_b, and parameter γ_b.

3. Radiative Transfer Simulation

Radiative transfer simulations were made with the Hydrolight 4.2 code[20] used to calculate the remote-sensing reflectance for a variety of water's optical properties. For simplicity, the water is taken in the simulations to be homogeneous and infinitely deep.

A. Inherent Optical Properties Model

The inherent optical properties required for the simulation are absorption coefficient a and volume scattering function $\beta(\Theta)$. For the present study the details of the absorption and scattering models are less important, provided that they cover realistic waters including case 2 waters. However, the SPF is crucial for determining the directional distribution.

For computation of an IOP, a four-component seawater model is considered. The four components are pure seawater, phytoplankton and their covarying particles, colored dissolved organic matter (CDOM), and noncovarying particles. In the notation for IOPs [a, b, b_b and $\beta(\Theta)$ or $P(\Theta)$] these components are indicated by subscripts w, C, CDOM, and NC, respec-

tively. In this water model, the total absorption coefficient is a sum of contributions from the four components:

$$a(\lambda) = a_w(\lambda) + a_C(\lambda) + a_{\mathrm{CDOM}}(\lambda) + a_{\mathrm{NC}}(\lambda). \quad (7)$$

The spectral data of a_w were taken from Pope and Fry[21] and Smith and Baker[22] for λ = 730–800 nm. The values of a_C are computed as a function of *Chl* by use of a model from Bricaud *et al.*[23] Spectral CDOM absorption is assumed as follows[24]:

$$a_{\mathrm{CDOM}}(\lambda) = a_{\mathrm{CDOM}}(443)\exp[-S_{\mathrm{CDOM}}(\lambda - 443)],$$

$$S_{\mathrm{CDOM}} = 0.014\ \mathrm{nm}^{-1}, \quad (8)$$

$$a_{\mathrm{CDOM}}(443) = (0.2 + 0.8f_a)a_C(443), \quad (9)$$

where an input parameter f_a is used to generate different CDOM absorption coefficients. The two values 0 and 1 were used for f_a; each yielded a different CDOM absorption coefficient for the same *Chl*.

The absorption of noncovarying particles has a similar spectral form to CDOM absorption with a slightly lower slope parameter:

$$a_{\mathrm{NC}}(\lambda) = a_{\mathrm{NC}}(443)\exp[-S_{\mathrm{NC}}(\lambda - 443)],$$

$$S_{\mathrm{NC}} = 0.011\ \mathrm{nm}^{-1}, \quad (10)$$

$$a_{\mathrm{NC}}(443) = (0.5 + 0.5f_a)(0.041/0.5)b_{\mathrm{NC}}(555). \quad (11)$$

Slope parameter S_{NC} is from Bricaud *et al.*,[23] where the value was derived for the absorption of nonalgal particles in case 1 waters. A recent analysis[25] gives a similar slope parameter for case 2 waters. The same input f_a in Eq. (9) is used to generate different absorption coefficients for the same $b_{\mathrm{NC}}(555)$. In Eq. (11), $a_{\mathrm{NC}}(443)$ is assumed to be proportional to $b_{\mathrm{NC}}(555)$, with the constant of proportionality derived by use of an absorption/suspended particulate matter (SPM) ratio[25] of 0.041 $\mathrm{m}^2\ \mathrm{g}^{-1}$, a scattering/SPM ratio[26] of 0.5 $\mathrm{m}^2\ \mathrm{g}^{-1}$, and variable input f_a. There is a slight discrepancy here from the cited literature, as the scattering/SPM ratio was measured for total particulate scattering in case 2 waters[26] but is used here only for noncovarying particles, assuming that the algal scattering is much smaller than the nonalgal scattering in case 2 waters. This discrepancy is, however, not important in this context because the underlying IOP model is used merely to simulate realistic reflectance spectra for generation of lookup tables with various total scattering/absorption ratios and not for IOP retrieval.

In a similar way, volume scattering function $\beta(\Theta)$ is composed of contributions from pure water (β_w), covarying particles (β_C), and noncovarying particles (β_{NC}):

$$\beta(\Theta) = \beta_w(\Theta) + \beta_C(\Theta) + \beta_{\mathrm{NC}}(\Theta). \quad (12)$$

Equation (12) can be rewritten in terms of scattering coefficients and phase functions:

$$bP(\Theta) = b_wP_w(\Theta) + b_CP_C(\Theta) + b_{\mathrm{NC}}P_{\mathrm{NC}}(\Theta). \quad (13)$$

Scattering coefficient b and SPF $P(\Theta)$ of the three components now need to be specified. Pure-water scattering coefficient b_w and its SPF, $P_w(\Theta)$, have been well studied.[27] The scattering coefficient of covarying particles,[28] b_C, is modeled as follows with n = 1:

$$b_C(\lambda) = 0.3\ Chl^{0.62}(550/\lambda)^n. \quad (14)$$

In contrast to pure-water scattering, the SPFs of the particles, $P_C(\Theta)$ and $P_{\mathrm{NC}}(\Theta)$, are not well established and show high variability for the same *Chl*, probably because of the diversity of the size distribution, refractive index, and shape anisotropy of particles. Use of a single SPF, $P_C(\Theta)$, for a wide range of *Chl* is incompatible with the observation that the backscattering ratio of case 1 water particles decreases as *Chl* increases.[3] This backscattering ratio has been modeled as a function of chlorophyll concentration from water reflectance measurements[3,4,29] or has been measured directly.[30] Note that measurements by Haltrin *et al.*[31] suggest that in turbid waters the backscattering ratio increases as *Chl* increases. However, such a different model of backscattering as a function of *Chl* does not significantly change the modeling accuracy of the final R_{rs} model if the particle backscattering coefficient is estimated correctly. For the simulations here, the dependence of the backscatter ratio of phytoplankton to covarying particles $\tilde{b}_{\mathrm{bC}} = b_{\mathrm{bC}}/b_C$ and *Chl* was assumed as

$$\tilde{b}_{\mathrm{bC}} = 0.012\ Chl^{-0.19}, \quad (15)$$

which was derived from R_{rs} and *Chl* data of the CalCOFI dataset [see Fig. 5(f) of Park *et al.*[32]]. From this equation $\tilde{b}_{\mathrm{bC}}$ has the values 0.018, 0.012, and 0.0075 for *Chl* values 0.1, 1, and 10 mg/m3, respectively, which is close to Morel's estimation[3] and also consistent with measurements.[30] To meet this requirement for the backscattering ratio we generate $P_C(\Theta)$ simply[2,32] by combination of two extreme phase functions, given by the Fournier–Forand (FF) analytic expressions.[33] The FF phase functions are based on Mie theory and give good fits to the measurements[34,35] over the wide range of scattering angles. Thus $P_C(\Theta)$ is generated from

$$P_C(\Theta) = r_1P_{\mathrm{FF1}}(\Theta) + (1 - r_1)P_{\mathrm{FF2}}(\Theta), \quad (16)$$

where $P_{\mathrm{FF1}}(\Theta)$ and $P_{\mathrm{FF2}}(\Theta)$ are the FF phase functions with backscattering ratios 0.03 and 0.002, respectively. Measurements of backscattering lie well between the two values.[30] We obtain $P_{\mathrm{FF1}}(\Theta)$ and $P_{\mathrm{FF2}}(\Theta)$ with the method described by Mobley *et al.*[35] by setting the refractive index–Junge slope pair (n_p,

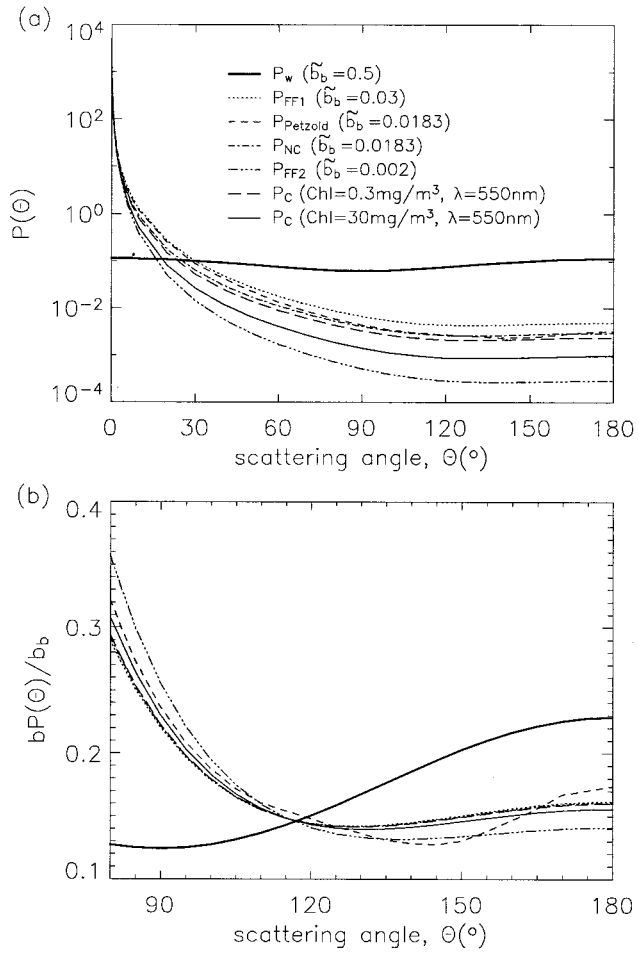

Fig. 1. SPFs of pure seawater and particles used in simulations: (a) SPFs for the entire range of scattering angles and (b) NSPFs for scattering angles of 80° to 180°. P_w is the SPF for pure seawater, P_C is the SPF for phytoplankton and related particles, and P_{NC} is the SPF for noncovarying particles; P_{FF1} and P_{FF2} are Fournier and Forand phase functions with backscattering ratios 0.03 and 0.002, respectively. P_C and P_{NC} are generated from P_{FF1} and P_{FF2} with appropriate mixing ratios to give the target backscattering ratios, $\tilde{b}_b = b_b/b$ (see text for details). The average of Petzold particle SPFs, $P_{PETZOLD}$, is also shown for comparison.

μ_J) to be (1.117, 3.695) and (1.050, 3.259), respectively. These two FF phase functions are shown in Fig. 1. Variable r_1 represents the fraction of $P_{FF1}(\Theta)$ in $P_C(\Theta)$, and we determine it for a given *Chl* by integrating Eq. (16) over the backscattering hemisphere:

$$0.03r_1 + 0.002(1 - r_1) = \tilde{b}_{bC}. \quad (17)$$

The scattering coefficient of noncovarying particles is assumed to follow the power law with $n = 1$:

$$b_{NC}(\lambda) = b_{NC}(550)(550/\lambda)^n. \quad (18)$$

Although this λ^{-1} law is often adopted for marine particles,[3,4] note that for the NC particles it could be slightly steeper than measurements.

We varied the particle scattering coefficient for specified *Chl* by using the factor *fb*(=0.5, 1, 2, 4, 8, 16):

$$b_C(550) = 0.3\ Chl^{0.62} f_b,$$

$$b_{NC}(550) = 0 \qquad (0 < f_b \le 1),$$

$$b_C(550) = 0.3\ Chl^{0.62},$$

$$b_{NC}(550) = 0.3\ Chl^{0.62}(f_b - 1) \qquad (f_b > 1). \quad (19)$$

The SPF of noncovarying particles, $P_{NC}(\Theta)$, is computed from the equation $P_{NC}(\Theta) = 0.583P_{FF1}(\Theta) + 0.417P_{FF2}(\Theta)$, which gives the same backscattering ratio as the Petzold particle phase function,[38,39] $P_{PETZOLD}(\Theta)$, for measurements made in San Diego Harbor, California. $P_{NC}(\Theta)$ and $P_{PETZOLD}(\Theta)$ are also shown in Fig. 1. A difference can be seen in Fig. 1(b) between $P_{NC}(\Theta)$ and $P_{PETZOLD}(\Theta)$ when they are normalized to a backscattering ratio. $P_{NC}(\Theta)$ is smoother than $P_{PETZOLD}(\Theta)$ for the backscattering angles: higher for Θ = 130°–165° and lower for Θ = 165°–180°. It is worth noting that SPF measurements are still subject to significant uncertainty. The angular shape of the SPF at backward-scattering angles can be critical for shaping the water-leaving radiance, especially when single scattering is dominant.

B. Input Parameters for Simulations

Remote-sensing reflectance was computed with the Hydrolight 4.2 code with the following input parameters:

- 10 wavelengths: 412, 443, 490, 510, 555, 565, 620, 665, 710, and 780 nm;
- 8 values for *Chl*: 0 (pure water), 0.03, 0.1, 0.3, 1, 3, 10, and 30 mg/m^3;
- 2 levels for absorption: f_a = 0, 1 (see text above for details);
- 6 levels for scattering: f_b = 0.5, 1, 2, 4, 8, 16 (see text above for details);
- 7 solar zenith angles: 0, 15°, 30°, 45°, 60°, 75°, and 85°;
- 10 sensor zenith angles: 0, 10°, 20°, 30°, 40°, 50°, 60°, 70°, 80°, and 87.5°;
- 13 relative azimuth angles: 0–180° at 15° intervals;
- wind speed: 0, 5, and 10 m/s for cloud-free skies; and
- cloud coverage: 0%, 50%, and 100% for a wind speed of 5 m/s.

These combinations of wavelength, *Chl*, f_a, and f_b give a wide range of absorption and backscatter. The absorption at 443 nm after exclusion of the pure-water contribution varies by as much as ~10 times that of a case 1 average model for a given *Chl*, as shown in Fig. 2. The backscatter at 555 nm after exclusion of the pure-water contribution varies by as

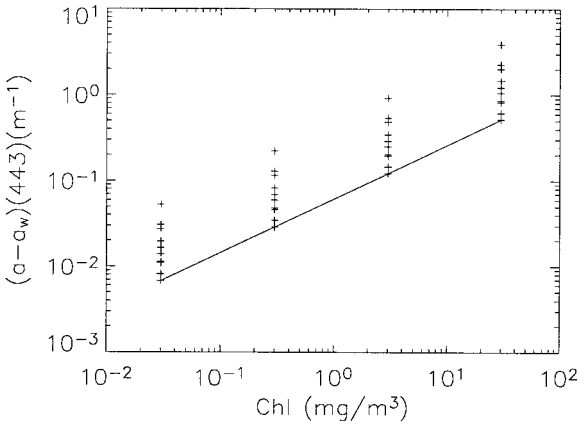

Fig. 2. Simulation conditions: absorption coefficients versus *Chl*. The symbols connected by the diagonal line show the case 1 average model with $f_a = 0$ and $b_{NC} = 0$ (see text for details).

much as ~15 times that of the lowest case for a given *Chl*, as shown in Fig. 3.

The γ_b values range from 0.2 to 1 except for the pure-water (*Chl* = 0 mg/m^3) case, as shown in Fig. 4. Low γ_b corresponds to a shorter wavelength with a small scattering factor, f_b. To minimize the model (lookup table) error we need to carry out simulations for grid values of γ_b: 0 (pure water), 0.2, 0.4, 0.6, 0.7, 0.8, 0.9, and 0.99. To simulate R_{rs} at these exact values of the γ_b grid we obtained the initial value of γ_b for given input parameters *Chl*, f_a, f_b, and wavelength and then reset it to the nearest grid value by adjustment of the absorption coefficient of the water body.

A wind speed of 5 m/s and a cloud-free sky are assumed, except where specified. Later in this paper the effects of cloud cover as well as of wind speed will be mentioned. A clear-sky radiance model of Harrison and Coombes[40] obtained with the Hydrolight 4.2 code has been used. Other atmospheric conditions such as sea-level pressure, relative humidity, horizontal visibility, and ozone concentration are described in the Hydrolight 4.2 technical documentation.[20]

Parameter ω_b reaches a maximum of 0.6 (0.3 for

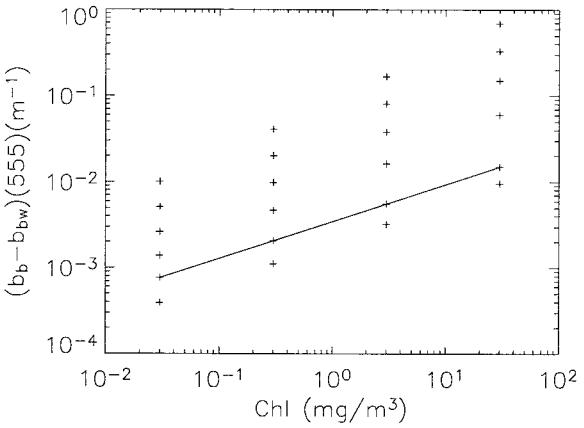

Fig. 3. Simulation conditions: backscattering coefficients versus *Chl*. Symbols connected by the diagonal line show a case 1 water model. See text for details.

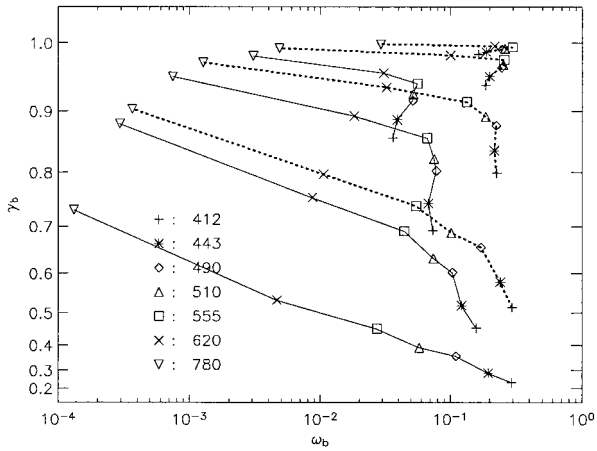

Fig. 4. Simulation conditions: γ_b versus ω_b. Solid curves, $f_b = 1$ (case 1 waters); dotted curves, $f_b = 4$ (see text). Either solid or dotted curves are, from the bottom, for *Chl* = 0.03, 0.3, 3.0, 30 mg/m^3.

$f_b = 4$ as shown in Fig. 4) for $\gamma_b = 0.99$ and varies in limited ranges (0–0.34) for the values of γ_b = 0.2–0.95. For $\gamma_b = 0.99$, ω_b is greater than 0.01 for all wavelengths used (Fig. 4).

4. Results and Analysis

A. Fourth-Order Polynomial Fitting of R_{rs} as a Function of ω_b

To prevent any confusion, the three angles used as model inputs are defined here: the solar (sensor) zenith angle is the angle between the zenith line pointing upward and the direction to the Sun (sensor); the relative azimuth angle is defined as the angle difference between the sensor azimuth angle and the solar azimuth angle. So $\Delta\phi = 0°$ if the sensor views along the retroreflecting direction and $\Delta\phi = 180°$ if sensor views along the mirror-reflecting direction.

Using the simulated R_{rs} data, we computed and tabulated coefficients g_i of Eq. (6) for the grid values of θ_0, θ, $\Delta\phi$, and γ_b described in Section 3. The number of data points used for fitting was 11, 114, 56, 60, 46, 82, 162, and 332 for $\gamma_b = 0$, 0.2, 0.4, 0.6, 0.7, 0.8, 0.9, 0.99, respectively. Chi-square fitting[41] was used with weights inversely proportional to R_{rs}. The coefficients g_i vary with Sun-sensor angle and γ_b: $g_1 = 0.03$–0.07, $g_2 = 0$–0.3, $g_3 = -0.8$–0.2, and $g_4 = -0.2$–1.0. Uncertainties in these coefficients were less than 3×10^{-5} for g_1, 0.0012 for g_2, 0.007 for g_3, and 0.009 for g_4 when 0.1% of R_{rs} simulation errors were assumed.

Figure 5 shows simulated R_{rs} data with fitting curves for four conditions of Sun and sensor angles. Different colors denote different values of γ_b. In general, R_{rs} is strongly correlated with ω_b, as known from the conventional models such as Eqs. (1) and (2). However, the value of R_{rs} for given values of IOPs (γ_b and ω_b in Fig. 5) does vary with Sun and sensor angles, as discussed below. There is also a significant dependence of R_{rs} on γ_b, which is the reason for use of γ_b as a model input. This γ_b dependence of R_{rs} could be

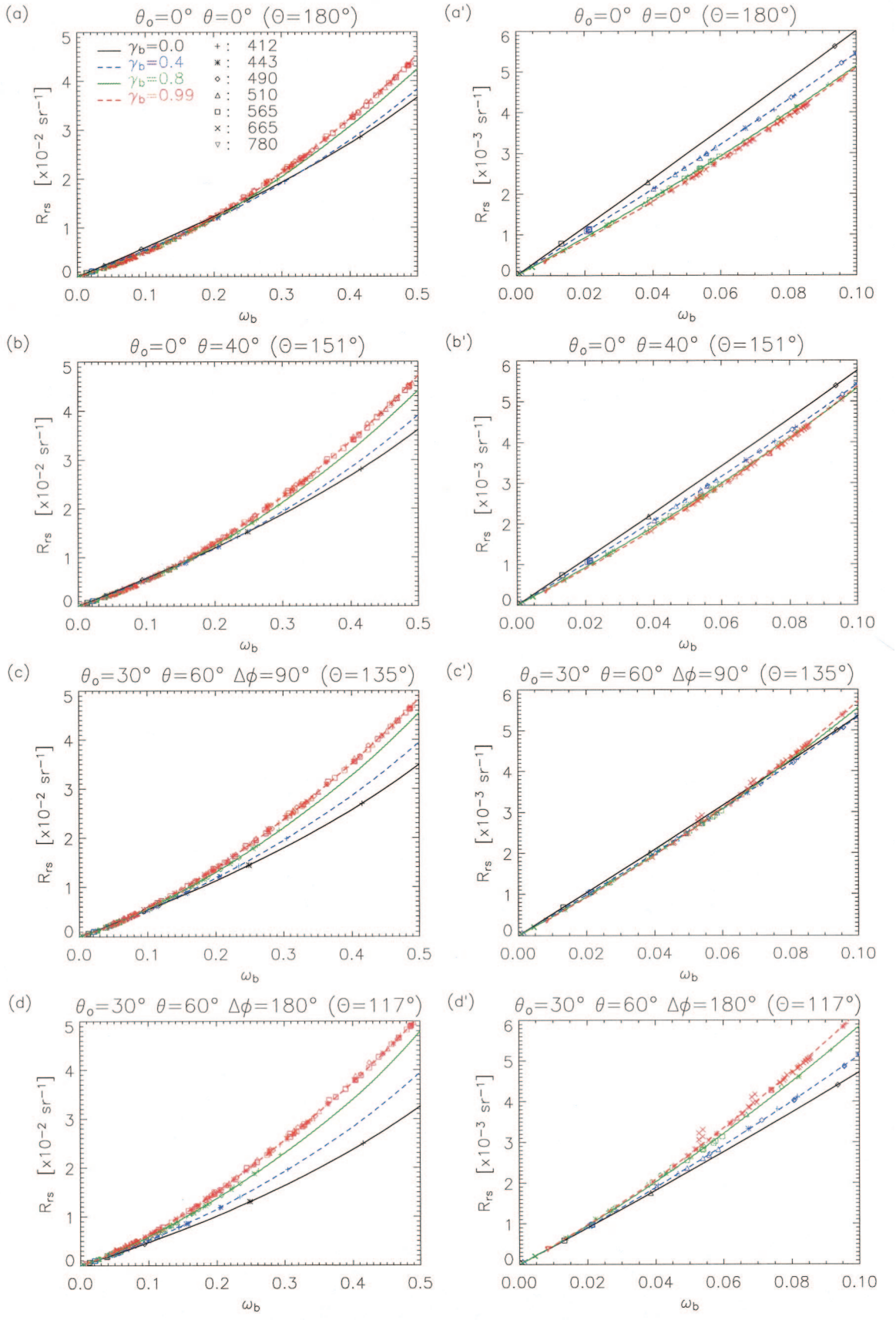

Fig. 5. R_{rs} versus ω_b for four Sun–sensor geometries. The values of Sun and sensor angles and corresponding scattering angles in water are given above the figures. Left, $0 < \omega_b < 0.5$; right, $0 < \omega_b < 0.1$. Simulated R_{rs} data are shown as symbols, and fitting curves are shown as solid curves. Different colors are for different values of γ_b, and different symbols are for different wavelengths.

explained in terms of SPF because γ_b determines the SPF as a first approximation. The value of the scattering angle in water, Θ, is given at the top of each of Figs. 5(a)–5(d′) to represent Sun and sensor angles in the interpretation.

This γ_b dependence of R_{rs} appears different according to the magnitude of ω_b, as can be seen from Fig. 5. For small $\omega_b(<0.02)$, R_{rs} decreases with γ_b for $\Theta > 120°$ [Figs. 5(a′), 5(b′), and 5(c′)] and increases with γ_b for $\Theta < 120°$ [Fig. 5(d′)]. On the contrary, for $\omega_b > 0.3$, higher γ_b gives consistently higher R_{rs} [Figs. 5(a), 5(b), 5(c), and 5(d)]. For convenience, these two ranges are considered separately. First, for $\omega_b < 0.02$, the average number of scattering events per photon,[19] n_p, is less than 2 ($\gamma_b = 0.4$) to 5 ($\gamma_b = 0.99$) when $r_{FF1} = 0.7$ (see Subsection 4.B below for the definition of r_{FF1}), and it is expected that single scattering will dominate or at least that multiple-scattering effects will be weak. Therefore, in this ω_b range, R_{rs} should reflect the detailed shape of the SPF at backward-scattering directions according to Eqs. (3) and (4). At large scattering angles ($\Theta \approx 150°$–$180°$), the value of the NSPF is large for water and small for particles [Fig. 1(b)]. As a result, for a given ω_b, smaller γ_b gives higher R_{rs}. This NSPF difference between water and particles becomes smaller as Θ approaches $\sim 120°$ [Fig. 1(b)]. Therefore the R_{rs} variation with γ_b is smaller in Figs. 5(c′) and 5(d′) than Figs. 5(a′) and (b′) for this small ω_b range ($\omega_b = 0.0$–0.02).

For $\omega_b = 0.3$, however, n_p ranges from ~ 30 ($\gamma_b = 0.4$) to 75 ($\gamma_b = 0.99$) when $r_{FF1} = 0.7$. For this ω_b value, multiple scattering is expected to be more important than the detailed shape of the NSPF at the corresponding scattering angle Θ in describing the γ_b dependence of R_{rs} because multiple scattering events with different scattering angles contribute to R_{rs} at scattering angle Θ. Furthermore, the high values of the NSPF at Θ smaller than 120° influence R_{rs} by multiple scattering. This intermediate angle (side) scattering explains why the curves of R_{rs} versus ω_b show greater upward curvature for high γ_b than for small γ_b, though all curves show upward curvature caused by multiple scattering. Therefore, variation in R_{rs} as a result of γ_b becomes larger as ω_b increases.

As the magnitudes of the single- and multiple-scattering effects on R_{rs} depend on the scattering angle, the value of ω_b where the R_{rs} variation that is due to γ_b is minimum also varies with the scattering angle: $\omega_b \approx 0.02$ for $\Theta = 117°$, $\omega_b = 0.06$ for $\Theta = 135°$, and $\omega_b = 0.2$ for $\Theta = 180°$. At a scattering angle of 135° [Fig. 5(c′)], the R_{rs} variation with γ_b that is due to variation of the NSPF (single scattering) and the variation that is due to multiple scattering approximately cancel, and R_{rs} is almost independent of γ_b for ω_b smaller than 0.1. This observation implies that R_{rs} values measured at $\Theta \approx 135°$ are less sensitive to the phase function variation if $R_{rs} < 0.05$ or $\omega_b < 0.1$. Finally, it can be seen that $\gamma_b = 0.99$ could be used for the relationship of R_{rs} and ω_b if $R_{rs} > 0.03$, which is consistent with neglecting the pure-water contribution to R_{rs} for highly turbid waters.[10]

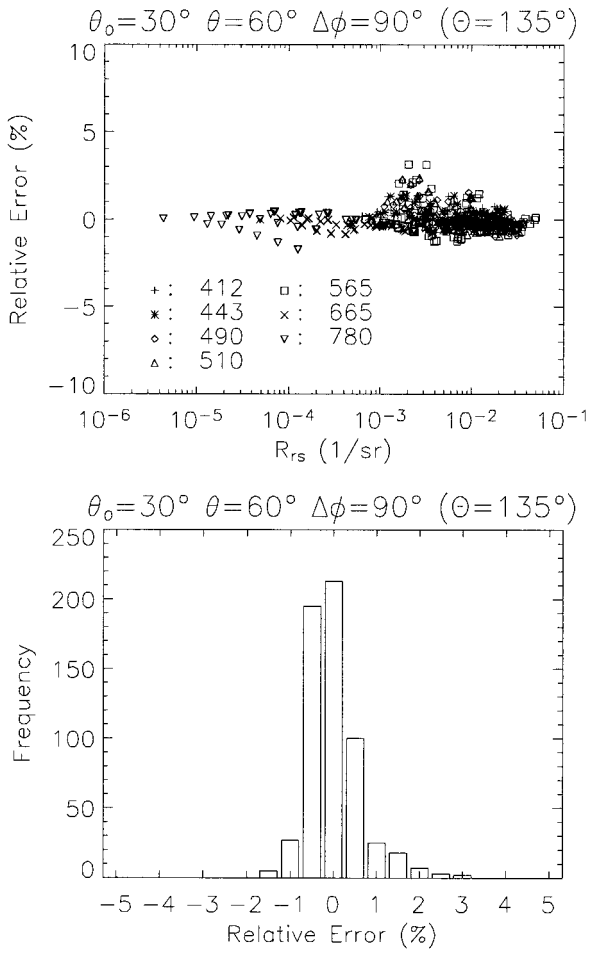

Fig. 6. Percentage difference of simulation from model R_{rs} (top) as a function of R_{rs} and (bottom) its histogram for a Sun-sensor geometry as shown.

B. Modeling Uncertainty and Particle Phase Function

Figure 5 shows that the use of parameter γ_b as a model input gives an important reduction of the model uncertainty compared to use of a fixed SPF. The difference of simulated R_{rs} from the fitting curve for one Sun–sensor configuration ($\theta_o = 30°$, $\theta = 60°$, and $\Delta\phi = 90°$) is shown in Fig. 6. The difference is typically $\pm 2\%$, with a few outliers greater than 3% and a root-mean-square difference of $\sim 1\%$ for various Sun and sensor angles. In Subsection 4.A, R_{rs} was modeled as function of ω_b for several values of parameter γ_b, the ratio of particulate backscattering to total backscattering. The γ_b parameter is the most important factor to influence the phase function and thus represents most of the variability of R_{rs} for any given ω_b and Sun–sensor geometry. However, there is still some variability of R_{rs} for given ω_b and γ_b because of the uncertainty in phase function that arises from different particle types. This phase function uncertainty together with imperfections in the use of Eq. (6) for curve fitting gives the total fitting uncertainty, which is shown in Fig. 6.

To show the effects of the particle phase function uncertainty on the R_{rs} modeling, we define another

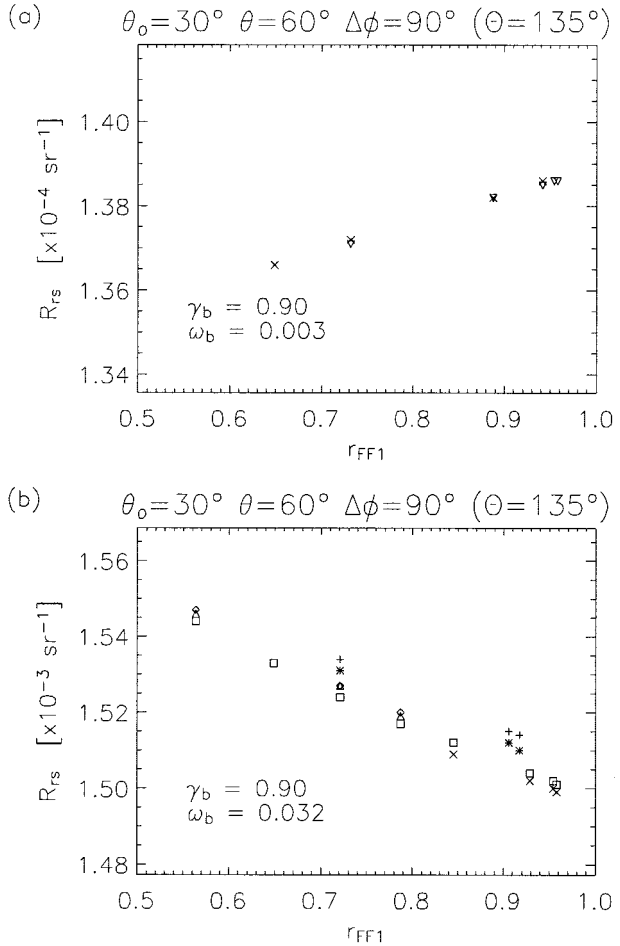

Fig. 7. Two contrasting examples of the R_{rs} variation as a function of r_{FF1} for certain values of ω_b and γ_b. The Sun and sensor angles are the same as those of Fig 6.

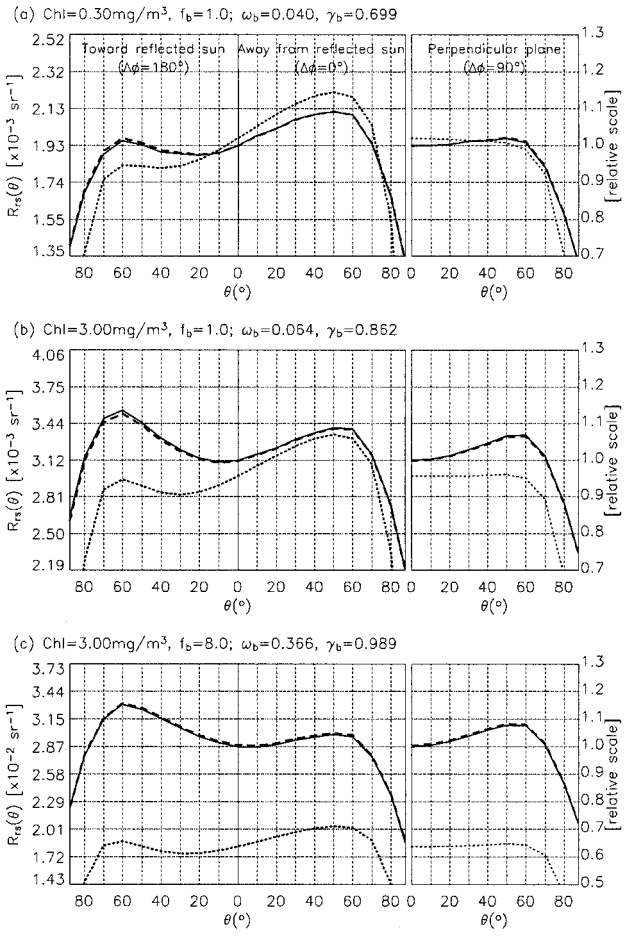

Fig. 8. Directional variation of R_{rs} for (a), (b) case 1 water and for (c) turbid water. Values of solar zenith (θ_o = 30°), wavelength (λ = 565 nm), and wind speed (W = 5.0 m/s) are the same for (a)–(c). Solid curves, data from Hydrolight simulations, dashed curves, data computed with the model of Eq. (5). For comparison, the QSSAs are shown as dotted curves.

parameter, r_{FF1}, to be the ratio of the FF1 particle backscatter to the total particle backscatter [$r_{FF1} = b_{b,FF1}/(b_{b,FF1} + b_{b,FF2})$]. Note that with the two parameters (γ_b and r_{FF1}), the total phase function of the water body is uniquely identified. r_{FF1} varies from 0.56 to 0.98 in the simulations. The low values of r_{FF1} correspond to a greater contribution from P_C (high *Chl*) than from P_{NC}; the high values of r_{FF1}, to a smaller contribution from P_C (low *Chl*) or a greater contribution from P_{NC} to the particle phase function. The simulated R_{rs} is shown in Fig. 7 relative to r_{FF1} for ω_b = 0.003 [Fig. 7(a)] and ω_b = 0.032 [Fig. 7(b)]. The value of γ_b is 0.9 for both figures. R_{rs} increases with r_{FF1} for ω_b = 0.003 [Fig. 7(a)], whereas R_{rs} decreases with r_{FF1} for ω_b = 0.032 [Fig. 7(b)]. This result can be explained with the same reasoning as was used in Subsection 4.B regarding the effects of scattering angle variation of phase function and of multiple scattering. n_p varies from 1.7 to 1.2 with varying r_{FF1} for ω_b = 0.003 and from 8 to 2.5 for ω_b = 0.032. For scattering angle Θ = 135°, the value of the NSPF for the FF1 particles is larger than for the FF2 particles, as shown in Fig. 1(b). Thus, in the single-scattering-dominated case [Fig. 7(a)], R_{rs} increases with r_{FF1}. Note, however, that single scattering dominates only for extremely small ω_b as in Fig. 7(a), because this NSPF variation that is due to r_{FF1} is a second-order effect compared with the variation that is due to γ_b. As multiple scattering increases, however, R_{rs} will be affected by the phase function for scattering angles smaller than 120°, where scattering by FF1 particles is smaller then scattering by FF2 particles. This variation of R_{rs} with r_{FF1} is ~1.5% in Fig. 7(a) and ~2.7% in Fig. 7(b). Figure 7(b) also shows ~1% of uncertainty with respect to wavelength. This uncertainty arises from the wavelength dependence of the skylight contribution to the illuminating radiance.

C. Bidirectional Distribution

Figure 8 shows the bidirectional distribution of R_{rs} for three cases: case 1 waters with *Chl* = 0.3 mg/m^3 [Fig. 8(a)] and with *Chl* = 3 mg/m^3 [Fig. 8(b)], and turbid case 2 water with *Chl* = 0.3 mg/m^3 and f_b = 8 [Fig. 8(c)]. R_{rs} increases generally as the sensor's zenith angle increases, which can be explained by the factor $1/(\mu_o + \mu)$ in Eq. (3), and R_{rs} decreases rapidly be-

yond a sensor zenith of 60° owing to a rapid decrease of sea-surface transmittance. In Fig. 8 the R_{rs} variations with sensor zenith are plotted in the principal plane that comprises Sun, zenith, and ground target and in the perpendicular plane, which is orthogonal to the principal plane. For sensor zeniths smaller than 60°, the variation in the principal plane is larger than that in the perpendicular plane because of a larger variation of the scattering angle. In this section, the variation in the principal plane is discussed for simplicity. The variation predicted by the QSSA [Eq. (3)] is shown by dotted curves for comparison.

The IOP conditions for Fig. 8(a) give γ_b of 0.699, indicating that pure water contributes 30% of total backscatter, and ω_b of 0.040. For this value of ω_b, single-scattering effects are expected to dominate the R_{rs} variation, especially near the retroreflecting direction ($\theta = 30°$, $\Delta\phi = 0°$). However, the simulation shows R_{rs} slightly lower than the QSSA (dotted curve). This difference arises from the wind-speed difference in the two computations. The simulation was made with a wind speed of 5 m/s, whereas the QSSA assumes a flat surface ($W = 0$ m/s). Corrected for this wind-speed effect, the QSSA approximates well the simulation on the right-hand half. For $\Delta\phi = 180°$ (viewing toward reflected Sun), multiple scattering accounts for ~10% for $40° \le \theta \le 60°$. This implies that, as far as directional variation is concerned, the multiple-scattering effects should be considered even if ω_b is relatively small.

Another case 1 water with *Chl* of 3 mg/m^3 [Fig. 8(b)] corresponds to higher values of γ_b and ω_b ($\gamma_b = 0.862$ and $\omega_b = 0.064$). A larger difference between simulation and QSSA can be seen. R_{rs} along the line for $\Delta\phi = 180°$ is much higher than QSSA, indicating that strong forward scattering significantly affects the R_{rs} distribution, especially for $\Delta\phi = 180°$, where the scattering angle is nearer to forward scattering.

Case 2 water with $Chl = 3$ mg/m^3 and $f_b = 8$ [Fig. 8(c)] corresponds to γ_b of 0.989 and ω_b of 0.366. The relative scale for this panel is changed for inclusion of the QSSA curve. This is a multiple-scattering-dominated case with a large contribution from particle backscatter. As in Fig. 8(b), the R_{rs} pattern is significantly different from the QSSA but now also for the retroreflection direction $\Delta\phi = 0°$. The variation along the $\Delta\phi = 0$ line of the principal plane is reduced. Thus the R_{rs} pattern has more asymmetry in the left and right halves than Figs. 8(a) and 8(b), indicating that the forward-scattering effects are stronger because of high values of ω_b and γ_b. In general, the directional variation was expected to be reduced for turbid waters. However, simulations for realistic waters where $\omega_b \le 0.6$ show that the directional variation is still significant, as was found previously.[10]

The value of R_{rs} obtained from Eq. (6) with coefficients fitted to the Hydrolight simulations are shown as dashed curves. The directional variation of R_{rs} is ~10%, which is 5 times higher than the model error of about 2% described above.

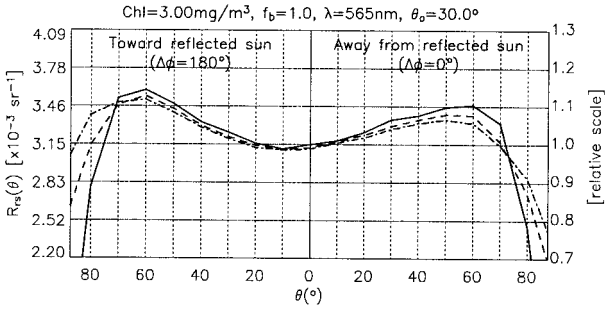

Fig. 9. Effects of wind speed on the R_{rs} variation in the principal plane. Solid, dashed, and dashed–dotted curves, $W = 0$, 5, 10 m/s, respectively.

Figure 9 shows the R_{rs} variation in the principal plane for wind speeds (W) of 0, 5, and 10 m/s. The simulation inputs are the same as in Fig. 8(b). The higher W gives lower R_{rs} for $\theta \le 60°$ and higher R_{rs} for $\theta \ge 70°$, though such a large zenith is not generally appropriate for remote sensing. The differences increase as the sensor's zenith angle approaches 60°, and R_{rs} at this angle for $W = 10$ m/s is ~4.9% lower than for $W = 0$ m/s. On the contrary, the subsurface's remote-sensing reflectances, r_{rs}, are within 1.6% for $\theta \le 60°$ (only a slight increase with wind speed, not shown here). This implies that the wind-speed effect on R_{rs} should be attributed at least partly to surface reflection [ρ in Eq. (4)], which is a function of θ and W. Preisendorfer and Mobley[42] showed that the surface reflectance for collimated light with an incident angle of water, θ_w, less than the critical angle (48.3°) increases with wind speed (see also Fig. 4.14 in Ref. 39), which can be associated with a decrease of R_{rs} for $\theta \le 60°$ with wind speed. It is also shown that the surface reflectance variation between $W = 0$ and 5 m/s is bigger than that between 5 and 10 m/s at $\theta_w = 40°$, i.e., $\theta = 60°$, which explains the larger variation of R_{rs} from 0 to 5 m/s at this sensor zenith.

The R_{rs} variation in the principal plane is shown in Fig. 10 for cloud coverage of 0%, 50% and 100% for the same simulation inputs as Fig. 8(b). As cloud coverage increases, the R_{rs} field becomes more symmetric. However, the variation with the sensor's zenith angle remains significant. The effect of homogeneous cloud coverage is minor if the cloud cover is less than 50%. This is convenient for process-

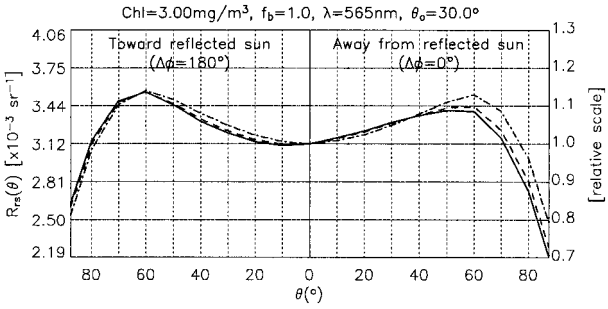

Fig. 10. Effects of cloud cover on R_{rs}. Solid, dashed, and dashed–dotted curves, 0, 50%, and 100% cloud cover, respectively.

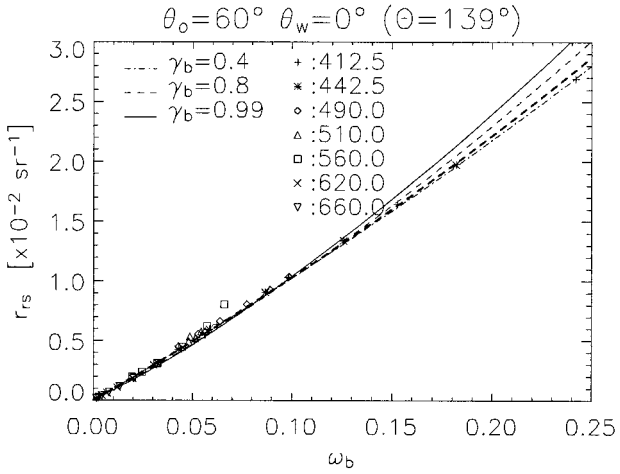

Fig. 11. Comparison of Eqs. (1) and (2) with the present model for subsurface remote-sensing reflectance r_{rs}. Thin curves are shown for three γ_b values; Eq. (1), as a thick dashed curve; and Eq. (2), as symbols. The data for symbols were computed with the f/Q table (without Raman scattering) of Morel *et al.*[2] for $\theta_o = 60°$ and $\theta = 0°$ and with the a and b_b model of Morel and Maritorena.[44]

ing of satellite ocean color data. However, the cloud effect on bidirectional reflectance should be considered for processing of seaborne or airborne R_{rs} measurements carried out in cloudy conditions, in addition to the effects of cloud coverage on air–sea interface reflection.[43]

5. Discussion

A. Comparison of the Present Model with Previous Models

The model presented in this study is compared to a case 1 water model for bidirectional reflectance,[2] which is referred to as the MAG02 model. The MAG02 model is given by Eq. (2) with bidirectional, *Chl*-dependent f/Q factors. This comparison is made for subsurface remote-sensing reflectance r_{rs} to prevent uncertainty in the sea–surface interface term because Eq. (2) is expressed in terms of the subsurface's remote-sensing reflectance. In Fig. 11 the present model (thin curves) and the MAG02 model (symbols) are shown for $\theta_o = 60°$ and $\theta = 0°$, and the ω_b range is limited to that covered by the MAG02 model. The model of Eq. (1) with $(l_1, l_2) = (0.0949, 0.0794)$ is shown as a thick, dashed curve. The data for the MAG02 model were computed by use of the f/Q table without Raman scattering[2] and with the models of a and b_b described by Morel and Maritorena.[44] Although the three models give similar results for ω_b smaller than 0.1 for this Sun–sensor geometry, the present model and the MAG02 model show a notable difference for a wavelength of 560 nm and *Chl* of 10 mg/m^3. This difference could be attributed to the difference in the SPFs used for the two models. Details of the SPFs used for the f/Q table can be found in Ref. 2. For ω_b larger than 0.15, however, the models of Eq. (1) and MAG02 are close to the low γ_b curves (low particle backscatter), which is reasonable because, in case 1 waters, such high ω_b corresponds to very low *Chl* at blue bands.

This comparison shows that the variability of r_{rs} that is due to the SPF variation in case 2 waters cannot be properly represented by either the case 1 water model or the simple model, Eq. (2) with constant coefficients (l_1, l_2).

B. Implications for Above-Water Measurements of Water-Leaving Reflectance for Satellite Validation

The bidirectional dependency of R_{rs} should be considered when the R_{rs} data measured with different instruments are compared. The sea-level validation of satellite water reflectance is one example of such a comparison in which satellite-derived reflectance is compared with seaborne measurements. For example, above-water R_{rs} measurements have been used for validation of Medium Resolution Imaging Spectrometer (MERIS) water reflectance for Belgian waters[45] for a sensor zenith of 40° and a relative azimuth of 45° to minimize the effects of ship shadow and Sun glint according to protocols described by Mueller *et al.*[46] The ratio of $R_{rs}(\theta_o = 30°, \theta = 40°, \Delta\phi = 45°)$ to $R_{rs}(\theta_o = 0°, \theta = 0°)$ is 1.052, 1.070, and 1.057 from simulations for Figs. 8(a), 8(b), and 8(c), respectively, and 1.054, 1.069 and 1.056 for the fitted model. This implies that the correction factor for bidirectional variation for $\theta_o = 30°$, $\theta = 40°$, and $\Delta\phi = 45°$ is 5–7% for these IOP conditions. Whereas uncertainties for satellite water-leaving reflectance in turbid coastal waters are generally much greater than 5%, especially at blue bands, these results suggest that an appropriate correction for the bidirectional effects will be necessary for achieving the stated 5% goal for water-leaving reflectance validation.[47] Similarly, the normalization of satellite measurements will need to be corrected for off-nadir viewing for underwater reflectance validation measurements.

C. Required Accuracy of b_b Estimation and Examples of Correction for Bidirectional Effects

The γ_b parameter is one of the entries in the lookup table of the model coefficients. This parameter must be estimated before the process for water-constituent retrieval is initiated. If b_b measurements are available, γ_b can be estimated. Otherwise, as in satellite data processing, b_b should be retrieved by iterations in a similar way to that proposed by Morel and Gentili[1] for *Chl* estimation for f/Q factor correction. Figure 12 shows the model predicted relation of R_{rs} and γ_b for three values of ω_b. From this figure it is assumed that the error in R_{rs} estimation, ΔR_{rs}, can be related to the error in γ_b estimation, $\Delta\gamma_b$, by

$$|\Delta R_{rs}|/R_{rs} \le 0.3/0.8\,|\Delta\gamma_b|. \quad (20)$$

If 2% uncertainty of R_{rs} estimation is required, which is approximately the same as the model uncertainty, the γ_b error should be smaller than 0.05. By definition of γ_b, $\Delta\gamma_b = \gamma_b(1 - \gamma_b)\Delta b_{bp}/b_{bp}$. From this equation, this γ_b error corresponds to a b_{bp} error of 20–30% for

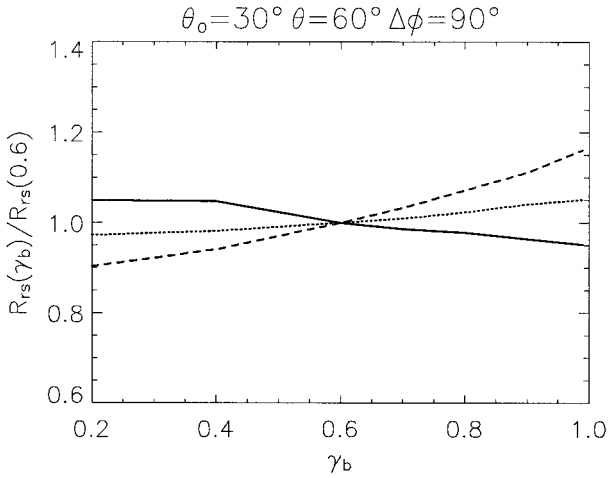

Fig. 12. Model predicted relation of R_{rs} versus γ_b for $\omega_b = 0.01$ (solid curve), 0.1 (dotted curve), and 0.3 (dashed curve).

$\gamma_b = 0.2\%$, 0.8 and of 55% and 105% for $\gamma_b = 0.9$, 0.95, respectively.

An iterative approach to the correction of bidirectional effects was implemented. With an initial value of $\gamma_b(\lambda)$, $R_{rs}(\theta_o, \theta, \Delta\phi)$ at 665 nm was converted to the ω_b parameter, $\omega_b(665)$. The *Chl* estimated by the OC4 algorithm[48] was used for $a_C(665)$ and $a_{CDOM}(443)$ {through $a_{CDOM}(665) = 0.5^* a_C(443)\exp[-0.014(665\text{-}443)]$}, which leads to total absorption, $a(665)$. Using these $\omega_b(665)$ and $a(665)$, we estimated $b_{bp}(665)$. This $b_{bp}(665)$ gives $b_{bp}(\lambda)$, assuming that $b_{bp}(\lambda)$ is proportional to $1/\lambda$, and thus a new $\gamma_b(\lambda)$ is obtained. This process is repeated until $\gamma_b(\lambda)$ converges. Figure 13 shows two examples of correction of the bidirectional effects by this iterative procedure. There are two groups of spectra: the lower curves show the correction of the spectrum $R_{rs}(\theta_o = 30°, \theta = 80°, \Delta\phi = 90°)$ simulated with $Chl = 0.3$ mg/m^3 and $f_b = 1$ (case 1 water), and the upper curves show the correction of the spectrum $R_{rs}(\theta_o = 30°, \theta = 60°, \Delta\phi = 90°)$ simulated with

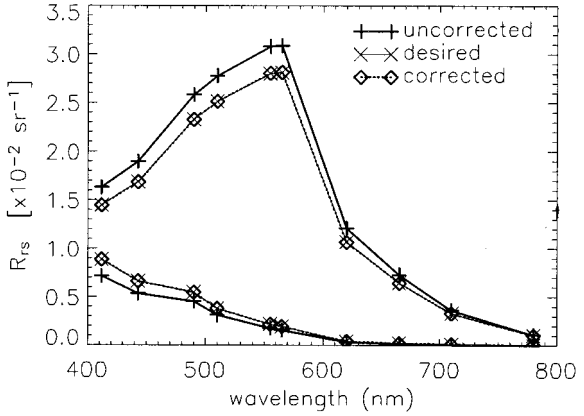

Fig. 13. Correction for the R_{rs} bidirectional effects: $R_{rs}(\theta_o = 30°, \theta = 80°, \Delta\phi = 90°)$ simulated with $Chl = 0.3$ mg/m^3 and $f_b = 1$ (bottom curves) and $R_{rs}(\theta_o = 30°, \theta = 60°, \Delta\phi = 90°)$ simulated with $Chl = 3$ and $f_b = 8$ (upper curves).

$Chl = 3$ and $f_b = 8$ (case 2 water). The corrected spectra are indistinguishable from the desired (target) spectra, $R_{rs}(\theta_o = 0°, \theta = 0°, \Delta\phi - 0°)$, indicating that the correction is perfect. Only two iterations were necessary to get to the stop condition that the average of $\gamma_b(\lambda)$ that is different from the previous iteration is less than 5%.

6. Conclusions

A model of remote-sensing reflectance (R_{rs}) has been presented that relates remote-sensing reflectance above the sea's surface to the inherent optical properties of a water body. This model was designed to represent the bidirectional properties of waters for which the backscatter coefficient is not determined entirely by *Chl*, thus extending the work of Morel and Gentili[1] and Morel *et al.*[2] The model requires Sun and sensor angles as input parameters to define the bidirectional variation. It also requires an additional parameter (γ_b, the contribution of suspended particles to the backscattering coefficient) to represent the variation of the scattering phase functions. To calibrate the model, we carried out systematic computations of R_{rs} by running the Hydrolight code for a variety of water properties.

The dependence of R_{rs} on γ_b for a Sun–sensor configuration (which corresponds to a scattering angle, Θ) has been analyzed and explained in terms of the variation of the scattering phase function. The scattering phase function at scattering angle Θ that corresponds to specific Sun and sensor angles largely explains the R_{rs} dependence on γ_b for ω_b smaller than 0.02–0.03 (single-scattering effect). However as ω_b increases, the scattering phase function at scattering angles smaller than Θ, where the scattering intensity is higher, has an increasing effect on determining R_{rs} (multiple-scattering effect). The relative strength of the single-scattering and multiple-scattering effects, which depends on scattering angle Θ, explains the bidirectional distribution of R_{rs}.

The absolute uncertainty of the model is generally less than 2%. This uncertainty comes mainly from the phase function uncertainty that remains after the value of γ_b is specified and, to a lesser extent, from the illuminating radiance distribution, which is wavelength dependent, and from imperfection of the fitting curves. This model uncertainty is acceptable for modeling and correction for bidirectional variation, which is ~10%. Even for extremely turbid waters the directional variation of reflectance is significant for variations in sensor zenith angle, as was found previously by Loisel and Morel.[10]

The effect of wind speed on bidirectional reflectance could be associated with corresponding variation of the surface reflectance for water-leaving radiances and was found to be small (<2%) for wind speeds greater than 5 m/s.

The effect of homogeneous cloud cover was also investigated. Little difference (<2%) was found for constant viewing geometry when the cloud cover varied from 0% to 50%. However, the angular variation

of reflectance remained considerable (~10%) for the 100% overcast case.

It has been demonstrated that a bidirectional reflectance correction suitable for case 2 waters, such as presented here, is necessary for seaborne validation of satellite-derived water-leaving reflectance if a validation uncertainty of 5% or less[43] is required.

The present model can be applied for a wide range of ω_b, regardless of wavelength, if inelastic scattering such as Raman scattering and CDOM fluorescence are neglected. However, as the scattering phase function is critical in determining the directional distribution, the scattering phase functions used in this study should be validated in the future.

The tabulated coefficients of the model described here are made available to the public on the Internet (http://www.mumm.ac.be/OceanColour/). This study was funded by the Belgian Science Policy Office's STEREO (Research Programme for Earth Observation) program in the framework of the Belcolour project SR/00/03 and by the European Space Agency's PRODEX (Programme de Développement d'Expériences scientifiques) contract 15190/01. H. Fukushima at Tokai University and other members of the Japanese Advanced Earth Observation Satellite-II/Global Imager project are thanked for encouraging this study. The comments provided by an anonymous referee helped to improve this work. Many comments provided by an anonymous referee helped to improve this paper.

References

1. A. Morel and B. Gentili, "Diffuse reflectance of oceanic waters. III. Implication of bidirectionality for the remote-sensing problem," Appl. Opt. **35,** 4850–4862 (1996).
2. A. Morel, D. Antoine, and B. Gentili, "Bidirectional reflectance of oceanic waters: accounting for Raman emission and varying particle scattering phase function," Appl. Opt. **41,** 6289–6306 (2002).
3. A. Morel, "Optical modeling of the upper ocean in relation to its biogenous matter content (case 1 waters)," J. Geophys. Res. C **93,** 10749–10768 (1988).
4. H. R. Gordon, O. B. Brown, R. H. Evans, J. W. Brown, R. C. Smith, K. S. Baker, and D. K. Clark, "A semianalytic radiance model of ocean color," J. Geophys. Res. D **93,** 10909–10924 (1988).
5. S. A. Garver and D. A. Siegel, "Inherent optical property inversion of ocean color spectra and its biogeochemical interpretation. 1. Time series from the Sagasso Sea," J. Geophys. Res. **102,** 18607–18625 (1997).
6. H. J. Gons, M. Rijkeboer, and K. G. Ruddick, "A chlorophyll-retrieval algorithm for satellite imagery (Medium Resolution Imaging Spectrometer) of inland and coastal waters," J. Plankton Res. **24,** 947–951 (2002).
7. A. Morel and B. Gentili, "Diffuse reflectance of oceanic waters. II. Bidirectional aspects," Appl. Opt. **32,** 6864–6879 (1993).
8. Z. Lee, K. L. Carder, C. D. Mobley, R. G. Steward, and J. S. Patch, "Hyperspectral remote sensing for shallow waters. I. A semianalytical model," Appl. Opt. **37,** 6329–6338 (1998).
9. J. C. Kitchen and J. R. V. Zaneveld, "On the noncorrelation of the vertical structure of light scattering and chlorophyll a in case I waters," J. Geophys. Res. C **95,** 20237–20246 (1990).
10. H. Loisel and A. Morel, "Non-isotropy of the upward radiance field in typical coastal (Case 2) waters," Int. J. Remote Sens. **22,** 275–295 (2001).
11. A. Albert and C. D. Mobley, "An analytical model for subsurface irradiance and remote sensing reflectance in deep and shallow case-2 waters," Opt. Express **11,** 2873–2890 (2003), http://www.opticsexpress.org.
12. G. F. Moore, J. Aiken, and S. J. Lavender, "The atmospheric correction of water colour and the quantitative retrieval of suspended particulate matter in Case II waters: application to MERIS," Int. J. Remote Sens. **20,** 1713–1733 (1999).
13. B. Nechad, V. D. Cauwer, Y. Park, and K. Ruddick, "Suspended particulate matter (SPM) mapping from MERIS imagery. Calibration of a regional algorithm for the Belgian coastal waters," in *Proceedings of the MERIS User Workshop,* ESA-SP 549 (European Space Research and Technology Centre, European Space Agency, Noordwijk, The Netherlands, 2004), Session 3.
14. K. Ruddick, F. Ovidio, and M. Rijkeboer, "Atmospheric correction of SeaWiFS imagery for turbid coastal and inland waters," Appl. Opt. **39,** 897–912 (2000).
15. H. R. Gordon, "Simple calculation of the diffuse reflectance of the ocean," Appl. Opt. **12,** 2803–2804 (1973).
16. H. R. Gordon and D. K. Clark, "Clear water radiances for atmospheric correction of coastal zone color scanner imagery," Appl. Opt. **20,** 4175–4180 (1981).
17. D. Stramski and D. A. Kiefer, "Light scattering by microorganisms in the open ocean," Prog. Oceanogr. **28,** 343–383 (1991).
18. A. Morel and Y. Ahn, "Optics of heterotrophic nanoflagellates and ciliates: a tentative assessment of their scattering role in oceanic waters compared to those of bacterial and algal cells," J. Mar. Res. **49,** 177–202 (1991).
19. A. Morel and B. Gentili, "Diffuse reflectance of oceanic waters: its dependence on Sun angles as influenced by the molecular scattering contribution," Appl. Opt. **30,** 4427–4438 (1991).
20. C. D. Mobley and L. K. Sundman, *Hydrolight 4.2 Technical Documentation* (Sequoia Scientific, Redmond, Wash., 2001).
21. R. M. Pope and E. S. Fry, "Absorption spectrum (380–700 nm) of pure water. II. Integrating cavity measurements," Appl. Opt. **36,** 8710–8723 (1997).
22. R. C. Smith and K. S. Baker, "Optical properties of the clearest natural waters (200–800 nm)," Appl. Opt. **20,** 177–184 (1981).
23. A. Bricaud, A. Morel, M. Babin, K. Allali, and H. Claustre, "Variations of light absorption by suspended particles with chlorophyll a concentration in oceanic (case 1) waters: analysis and implications for bio-optical models," J. Geophys. Res. C **103,** 31033–31044 (1998).
24. A. Bricaud, A. Morel, and L. Prieur, "Absorption by dissolved organic matter of the sea (yellow substance) in the UV and visible domains," Limnol. Oceanogr. **26,** 43–53 (1981).
25. M. Babin, D. Stramski, G. M. Ferrari, H. Claustre, A. Bricaud, G. Obolensky, and N. Hoepffner, "Variations in the light absorption coefficients of phytoplankton, nonalgal particles, and dissolved organic matter in coastal waters around Europe," J. Geophys. Res. C **108,** 4-1–4-19 (2003).
26. M. Babin, A. Morel, V. Fournier-Sicre, F. Fell, and D. Stramski, "Light scattering properties of marine particles in coastal and open ocean waters as related to the particle mass concentration," Limnol. Oceanogr. **48,** 843–859 (2003).
27. A. Morel, "Optical properties of pure water and pure sea water," in *Optical Aspects of Oceanography*, N. G. Jerlov and E. S. Nielsen, eds. (Academic, New York, 1974), Chap. 1.
28. H. R. Gordon and A. Morel, "Remote assessment of ocean color for satellite visible imagery. A review," in *Lecture Notes on Coastal and Estuarine Studies*, R. T. Barber, C. N. K. Mooers, M. J. Bowman, and B. Zeizschel, eds. (Springer-Verlag, New York, 1983), pp. 1–114.

29. O. Ulloa, S. Sathyendranath, and T. Platt, "Effect of the particle-size distribution on the backscattering ratio in seawater," Appl. Opt. **33,** 7070–7077 (1994).
30. M. S. Twardowski, M. Boss, J. B. Macdonald, W. S. Pegau, A. H. Barnard, and J. R. V. Zaneveld, "A model for estimating bulk refractive index from the optical backscattering ratio and the implication for understanding particle composition in case I and case II waters," J. Geophys. Res. C **106,** 14129–14142 (2001).
31. V. I. Haltrin, M. E. Lee, E. B. Shybanov, R. A. Arnone, A. D. Weidemann, V. I. Mankovsky, W. S. Pegau, and S. D. Ladner, "Relationship between backscattering and beam scattering coefficients derived from new measurements of light scattering phase functions," in *Proceedings of Ocean Optics XII* (Institute of Electrical and Electronics Engineers, Piscataway, N.J., 1994).
32. Y.-J. Park, M. Kahru, and B. Mitchell, "Inversion modeling optimization using CalCOFI data set," in *Hypespectral Remote Sensing of the Ocean*, R. Frouin, H. Kawamura, and M. Kishino, eds., Proc. SPIE **4154,** 105–114 (2000).
33. G. Fournier and J. L. Forand, "Analytic phase function for ocean water," in *Ocean Optics XII*, J. S. Jaffe, ed., Proc. SPIE **2258,** 194–201 (1994).
34. V. I. Haltrin, "An analytic Fourier–Forand scattering phase function as an alternative to the Henyey–Greenstein phase function in hydrologic optics," in *1998 IEEE International Geoscience and Remote Sensing Symposium II*, T. I. Stein, ed. (Institute of Electrical and Electronics Engineers, Piscataway, N.J., 1998), pp. 910–912.
35. C. D. Mobley, L. K. Sundman, and E. Boss, "Phase function effects on oceanic light fields," Appl. Opt. **41,** 1035–1050 (2002).
36. A. H. Barnard, W. S. Pegau, and J. R. V. Zaneveld, "Global relationships of the inherent optical properties of the oceans," J. Geophys. Res. C **103,** 24955–24968 (1998).
37. R. W. Gould, R. A. Arnone, and P. M. Martinolich, "Spectral dependence of the scattering coefficient in case 1 and case 2 waters," Appl. Opt. **38,** 2377–2383 (1999).
38. T. J. Petzold, "Volume scattering functions for selected ocean waters," Tech. Rep. SIO 72-78 (Scripps Institution of Oceanography, San Diego, La Jolla, Calif., 1972).
39. C. D. Mobley, *Light and Water: Radiative Transfer in Natural Waters* (Academic, San Diego, Calif., 1994).
40. A. W. Harrison and C. A. Coombes, "An opaque cloud cover model of sky short wavelength radiance," Sol. Energy **41,** 387–392 (1988).
41. W. H. Press, S. A. Teukolsky, W. T. Vetterling, and B. P. Flannery, *Numerical recipes in C: The Art of Scientific Computing, 2nd ed.* (Cambridge U. Press, New York, 1992), Chap. 15.
42. R. W. Preisendorfer and C. D. Mobley, "Unpolarized irradiance reflectances and glitter patterns of random capillary waves on lakes and seas, by Monte Carlo simulation," NOAA Tech. Memo. ERL PMEL-63 (Pacific Marine Environmental Laboratory, Seattle, Wash., 1985).
43. C. D. Mobley, "Estimation of the remote-sensing reflectance from above-surface measurements," Appl. Opt. **38,** 7442–7455 (1999).
44. A. Morel and S. Maritorena, "Bio-optical properties of oceanic waters: a reappraisal," J. Geophys. Res. C **106,** 7163–7180 (2001).
45. K. Ruddick, V. D. Cauwer, Y. Park, G. Becu, J.-P. D. Blauwe, E. D. Vreker, P.-Y. Deschamps, M. Knockaert, B. Nechad, A. Pollentier, P. Roose, D. Saudemont, and D. V. Tuyckom, "Preliminary validation of MERIS water products for Belgian coastal waters," in *Proceedings of Envisat Validation Workshop,* SP-531 (European Space Research and Technology Centre, European Space Agency, Noordwijk, The Netherlands, 2003).
46. J. L. Mueller, C. Davis, R. Arnone, R. Frouin, K. Carder, Z. P. Lee, R. G. Steward, S. Hooker, C. D. Mobley, and S. McLean, "Above-water radiance and remote-sensing reflectance measurements and analysis protocols," in *Ocean Optics Protocols for Satellite Ocean Color Sensor Validation,* Rev. 2 (National Aeronautical and Space Administration, Greenbelt, Md., 2000), pp. 98–107.
47. S. B. Hooker, G. Lazin, G. Zibordi, and S. McClean, "An evaluation of above- and in-water methods for determining water-leaving radiances," J. Atmos. Ocean. Technol. **19,** 486–515 (2002).
48. J. E. O'Reilly, S. Maritorena, B. G. Mitchell, D. A. Siegel, K. L. Karder, S. A. Garver, M. Kahru, and C. McClain, "Ocean color chlorophyll algorithms for SeaWiFS," J. Geophys. Res. **102,** 18607–18625 (1998).